

CHAPTER 7

SURFACE TEMPERATURE

7.1 *Sea Surface Temperature Determination*

Much of what has been presented so far has assumed knowledge of the surface temperature. In this section, techniques to determine surface temperature are discussed.

In the infrared, the emissivity of the earth's sea and land surface is near unity. As a result, in the absence of cloud or atmospheric attenuation, the brightness temperature observed with a space-borne window radiometer is equal to surface skin temperature. However, cloud and water vapour absorption usually prohibit direct interpretation of the window channel data so that algorithms need to be applied to the data to alleviate the influence of clouds and water vapour absorption. The algorithms and instrumental approach have evolved from the use of a single window channel on a polar orbiting satellite to the use of multispectral radiometer observations from both polar orbiting and geostationary satellites.

The earliest single channel approach involved a statistical histogram of brightness temperatures that was used to distinguish cloud free observations from cloud contaminated observations and to obtain sea surface temperature measurements. The following assumptions are implicit in the technique: (a) sea surface temperature is slowly varying, so cloud free infrared window measurements over the sea will be very repetitive and sea surface brightness temperature values will have a high frequency of occurrence, and (b) cloud contamination will produce lower brightness temperature values than sea surface and the cloud brightness temperatures will be highly variable over an area due to variations in cloud amount, opacity, and altitude.

A typical histogram situation is shown in Figure 7.1. Part A shows the normal distribution obtained when all measurements are cloud free and no SST gradient exists. Part B, on the other hand, illustrates the situation when more than half of the samples are cloud contaminated. Since the cloud-contaminated radiance temperatures are lower than the cloud free temperatures, they populate the left hand side of the histogram, but also distribute themselves normally. Only the warm side of the normal density curve formed by cloud free observations can be distinguished from the combined data in the histogram. Since the mean of the normal (Gaussian) density function (probability function) formed from clear observations is the most likely value of the SST, several schemes have been developed to infer the mean of a Gaussian probability function from knowledge of the standard deviation S of the density function and knowledge of the geometry of one side of the distribution.

7.1.1 Slope Method

The slope method assumes that the brightness temperature frequency distribution is a normal function of the form

$$f(T) = f_s \exp [-(T - T_s)^2 / 2\sigma^2]$$

where f is the frequency of occurrence, $f_s = f(T_s)$ is unknown, the standard deviation S is assumed to be known from the characteristics of the measuring instrument, and the mean temperature T_s is the quantity to be determined. Since the standard deviation of a normal probability density function occurs at the inflection points on the curve, then

$$T_s = T_{\max} - \sigma$$

where T_{\max} is the solution of

$$d^2f/dT^2 = 0 ,$$

and S is determined from the equation

$$\sigma = (\sigma_N^2 + \sigma_E^2)^{1/2} ,$$

where σ_N and σ_E are the standard deviations, respectively, of the instrument noise and the expected variance of the SST's.

7.1.2 Three Point Method

The three point method also assumes a normal probability function, and solves for T_s by selecting three points (T_i, f_i) , (T_j, f_j) , and (T_k, f_k) on the warm side of the histogram as follows

$$f_i = f_s \exp [-(T_i - T_s)^2/2\sigma^2]$$

$$f_j = f_s \exp [-(T_j - T_s)^2/2\sigma^2]$$

$$f_k = f_s \exp [-(T_k - T_s)^2/2\sigma^2] .$$

These three equations contain three unknowns f_s , σ , and T_s and can be solved by simple Gaussian elimination. Therefore

$$\ln(f_i/f_j) = [(T_i^2 - T_j^2) - 2T_s(T_i - T_j)]/2\sigma^2 ,$$

$$\ln(f_i/f_k) = [(T_i^2 - T_k^2) - 2T_s(T_i - T_k)]/2\sigma^2 ,$$

or, finally,

$$T_s = \frac{T_i \ln(f_j/f_k) - T_j \ln(f_i/f_k) + T_k \ln(f_i/f_j)}{2 [T_i \ln(f_j/f_k) - T_j \ln(f_i/f_k) + T_k \ln(f_i/f_j)]}$$

Since a single calculation of T_s can be influenced by noise and by the combination of the three points being slightly non-Gaussian, repeated calculations of T_s are made from all possible unique combinations of three points on the warm side of the histogram. Thus, if there are n useful points on the warm side, then all possible combinations ($i = 1, \dots, n - 2$; $j = i + 1, \dots, n - 1$; and $k = j + 1, \dots, n$) are used to construct a second histogram, called the mean estimate histogram from which the most frequently occurring estimate is taken as the correct one.

7.1.3. Least Squares Method

Another solution is through a least squares fit of the normal distribution probability function to three or more points on the warm end of the observed frequency distribution. It follows from before that

$$\ln(f(T)) = \ln(f_s) - T_s^2/2\sigma^2 + T_s T/\sigma^2 - T^2/2\sigma^2$$

which has the form

$$\ln(f(T)) = A_0 + A_1 T + A_2 T^2 ,$$

where

$$T_s = -A_1/(2A_2) ,$$

and

$$\sigma^2 = -1/(2A_2) .$$

Thus, given three or more points (f_i, T_i) on the cloud free portion of the histogram, one can solve for T_s and σ using the least squares solution.

7.2 Water Vapour Correction for SST Determinations

Several multispectral methods have evolved to correct for the presence of clouds in the area of interest. The detection of clouds was addressed more fully in the previous chapter. Correction for the effects of water vapor in the atmosphere is addressed here. The brightness temperature observed with a satellite radiometer can be equated to surface skin temperature after the effect of atmospheric water vapour absorption has been taken into account.

The surface temperature can be expressed in terms of the observed clear sky window channel brightness temperature, T_b , and a water vapour correction, T_c ;

$$T_s = T_b + T_c.$$

The water vapour correction ranges from a few tenths of a degree Kelvin in very cold and dry atmospheres to nearly 10 K in very warm and moist atmospheres for 11 micron window observations. The corresponding corrections for the 3.7 micron window are about half as large. The water vapour correction is highly dependent on wavelength. To see why this is so, consider that at 3.7 micron, the Planck radiance varies with temperature to approximately the thirteenth power whereas at 11 micron the Planck radiance varies with temperature to approximately the fourth power. Inserting

$$B_\lambda(T) = T^{n\lambda}$$

$$T_b \sim \tau_\lambda(p_s) T_s^{n\lambda} + (1 - \tau_\lambda(p_s)) T_a^{n\lambda}$$

where $\tau_\lambda(p_s)$ is the atmospheric transmittance, T_s is the surface temperature, and T_a is the mean atmospheric temperature. Assuming representative values of 0.8, 300 K, and 270 K for τ_s , T_s , and T_a , respectively, one finds that at 3.7 micron where $n_\lambda = 13$, the brightness temperature observed is 296.5 K as opposed to a value of 294.5 K observed at 11 micron where $n_\lambda = 4$. Clearly for a non-isothermal condition and the same atmospheric transparency, the water vapour correction does depend on wavelength. Figure 7.2a illustrates the water vapour corrections derived for the Nimbus-2 3.7 micron region due to the Planck radiance dependence discussed above. Note also the dependence of the water vapour correction on viewing angle.

The water vapour correction is best evaluated by observing the area of interest in multiple infrared window channels. In the atmospheric window regions, the absorption is weak, so that

$$\tau_w = e^{-k_w u} \sim 1 - k_w u$$

where w denotes the window channel wavelength, and

$$d\tau_w = -k_w du$$

What little absorption exists is due to water vapour, therefore, u is a measure of precipitable water vapour. The RTE can be written in the window region

$$I_w = B_{sw} (1 - k_w u_s) + k_w \int_0^{u_s} B_w du$$

u_s represents the total atmospheric column absorption path length due to water vapour, where s denotes surface. Defining an atmospheric mean Planck radiance

$$\bar{B}_w = \frac{\int_0^{u_s} B_w du}{\int_0^{u_s} du}$$

then

$$I_w = B_{sw} (1 - k_w u_s) + k_w u_s \bar{B}_w.$$

Since B_{sw} is close to both I_w and B_w , first order Taylor expansion about the surface temperature T_s allows us to linearize the RTE with respect to temperature, so

$$T_{bw} = T_s (1 - k_w u_s) + k_w u_s \bar{T}_w,$$

where \bar{T}_w is the mean atmospheric temperature corresponding to B_w . For two window channel wavelengths (11 and 12 micron) the following ratio can be determined.

$$\frac{T_s - T_{bw1}}{T_s - T_{bw2}} = \frac{k_{w1} u_s (T_s - \bar{T}_{w1})}{k_{w1} u_s (T_s - \bar{T}_{w2})}$$

Assuming that the mean atmospheric temperature measured in the one window region is comparable to that measured in the other, $\bar{T}_{w1} \sim \bar{T}_{w2}$, we can simplify to

$$\frac{T_s - T_{bw1}}{T_s - T_{bw2}} = \frac{k_{w1}}{k_{w2}}$$

from which it follows that

$$T_s = T_{bw1} + \frac{k_{w1}}{k_{w2} - k_{w1}} [T_{bw1} - T_{bw2}]$$

This is the split window channel expression for the water vapour correction to the SST. The term split window is used to denote two neighbouring channels in a relatively transparent or window region of the spectrum; one channel for which the atmosphere is highly transparent and the other for which atmospheric water vapour partially absorbed the surface radiance to space. For three window channels (at 3.7, 11, and 12 mm) the analogous expression is

$$T_s = T_{bw1} + \frac{k_{w1}}{2(k_{w2} - k_{w1})} [T_{bw1} - T_{bw2}] + \frac{k_{w1}}{2(k_{w3} - k_{w1})} [T_{bw1} - T_{bw3}]$$

Figure 7.2b provides a graphical representation of the multispectral window channel water vapour correction algorithm. This linear extrapolation technique was first proposed by Anding and Kauth (1970) and initially tested by Prabhakara *et al* (1974). Accuracies of 1.0-1.5 C absolute and 0.5-1.0 C relative have been routinely achieved in the last few years.

Recently, a more sophisticated algorithm for atmospheric correction has been adopted. It includes a nonlinear term to account for absorption of water vapor in very wet atmospheres. Thus a quadratic term is added to the regression, as suggested by McMillin and Crosby (1984). The regression equation to correct for atmospheric absorption and re-emission has the form:

$$\text{SST} = A_0 + A_1 \cdot T_{11} + A_2 \cdot T_{12} + A_3 \cdot dT^2$$

where $dT = T_{11} - T_{12}$. Table 7.1 summarizes the coefficients applicable to recent multispectral sensors.

The operational satellites currently in use for the SST determinations are the TIROS-N and GOES. The TIROS-N Advanced Very High Resolution Radiometer as well as the High resolution Infrared Sounder (HIRS) are well-suited to measure surface temperatures since they detect radiation in the split window (water vapour absorption and window channels). However, observations from the TIROS-N series of satellites are not always timely (overpasses occur only four times per day over any given region). On the other hand, the GOES Imager offers half hourly images at 4 km resolution (an order of magnitude more measurements of a given ocean surface). Thus, timely observations are available and the influence of clouds can often be alleviated by simply waiting for them to move out of the area of interest. Also, a given geographical region is always observed from the same viewing angle with the GOES Imager so that relative variations of observed surface temperature variations rather than to variations in scan geometry. With multispectral window radiometer data routinely available from the geostationary GOES, it is now possible to perform both precise water vapour correction and cloud filtering through quasi-continuous sampling with just one instrument.

The GOES cloud screening includes temporal continuity along with threshold tests with moisture corrected atmospheric infrared windows and visible reflectances. The following tests are used in the GOES SST algorithm for cloud detection.

$T_{11} > 270 \text{ K}$	ocean rarely frozen
$T_{11} > T_{12} + 4 \text{ K}$	clouds affect moisture correction
$\text{vis} < 4\%$	clouds reflect more than ocean sfc
$T_{11} - T_{3.9} > 1.5 \text{ K}$	subpixel clouds
$\Delta T_{11} < 0.3 \text{ K}$	ΔSST over 1 hr small
$-2 \text{ K} < \text{SST} - \text{guess} < 5 \text{ K}$	ΔSST over days bounded

GOES SSTs have been routinely generated every three hours in the vicinity of the continental USA since May 1997. The diurnal changes in the GOES SST are noticeable. As an example, Fig. 7.3a shows a three-day composite of the GOES SST around 1200 UTC (early morning), May 20-22, 1998, and Fig. 7.3b shows the difference eight hours later. The magnitude of the difference and the spatial distribution of the SST diurnal variation are remarkable. Variations as large as 3°K are found near the coast, where land contamination is a possible factor, and in regions where the surface wind is weak. Adequate validation and monitoring of such diurnal variations in surface skin temperatures is necessary; the implications if verified are many.

Climate analysis of SST may be vulnerable to the variable sampling times of polar orbiting satellites. A sun-synchronous polar orbiting satellite passes a given geographical location at similar local times each day, nominally shortly after noon and midnight, to measure SST. In the presence of SST diurnal variation, if clouds at a location tend to appear at one of these times (say afternoon), the climatology will be biased towards the other time (nighttime SST). If clouds tend to appear at both times, the SST climatology must be estimated from other data. If the cloud diurnal variation varies seasonally, say clouds tend to appear in the afternoon in summer but not in winter, the SST will be biased towards the nighttime SST in summer but not in winter.

7.3 Accounting for Surface Emissivity in the Determination of SST

When the sea surface emissivity is less than one, there are two effects that must be

considered: (a) the atmospheric radiation reflects from the surface; and (b) the surface emission is reduced from that of a blackbody. The radiative transfer can be written

$$I_{\lambda} = \varepsilon_{\lambda} B_{\lambda}(T_s) \tau_{\lambda}(p_s) + \int_0^{p_s} B_{\lambda}(T(p)) d\tau_{\lambda}(p) \\ + (1-\varepsilon_{\lambda}) \tau_{\lambda}(p_s) \int_0^{p_s} B_{\lambda}(T(p)) d\tau'_{\lambda}(p)$$

where $\tau'_{\lambda}(p)$ represents the transmittance down from the atmosphere to the surface. As before in the derivation of the microwave RTE, this can be derived in terms of the transmittance up through the atmosphere to the top, $\tau_{\lambda}(p)$. Then as before

$$I_{\lambda} = \varepsilon_{\lambda} B_{\lambda}(p_s) \tau_{\lambda}(p_s) + \int_{p_s}^0 B_{\lambda}(T(p)) F_{\lambda}(p) d\tau_{\lambda}(p)$$

where

$$F_{\lambda}(p) = \left\{ 1 + (1 - \varepsilon_{\lambda}) \left[\frac{\tau_{\lambda}(p_s)}{\tau_{\lambda}(p)} \right]^2 \right\}.$$

Assuming that the atmosphere is a single layer whose temperature T_A is the same for both upwelling radiance at the top of the atmosphere and the downwelling at the sea surface, then

$$I_{\lambda} = \varepsilon_{\lambda} B_{\lambda}(p_s) \tau_{\lambda}(p_s) + B_{\lambda}(T_A) [1 - \tau_{\lambda}(p_s) - (1 - \varepsilon_{\lambda}) \tau_{\lambda}(p_s)^2 + (1 - \varepsilon_{\lambda}) \tau_{\lambda}(p_s)]$$

or

$$I_{\lambda} = \varepsilon_{\lambda} B_{\lambda}(p_s) \tau_{\lambda}(p_s) + B_{\lambda}(T_A) [1 - \varepsilon_{\lambda} \tau_{\lambda}(p_s) - \tau_{\lambda}(p_s)^2 + \varepsilon_{\lambda} \tau_{\lambda}(p_s)^2].$$

Note that as the atmospheric transmittance approaches unity, the atmospheric contribution expressed by the second term becomes zero.

Figure 7.4 shows a plot of the window radiance data observed from an interferometer at ship level and at 20 km altitude in the atmosphere, as well as the GOES satellite radiometer. Figure 7.5 plots these radiances as a function of the correction term. The intercept of a regression line through these data is the Planck radiance corresponding to the sea surface temperature. In order to alleviate any scatter produced by the Planck radiance dependence on wavelength (or wavenumber), the observed radiances I_{λ} are converted to brightness temperature and then back to radiances for a reference wavelength λ_0 . The emissivity values are taken from the literature (Masuda *et al*, 1988) and the transmittance values are computed from a line by line model in conjunction with an in situ radiosonde profile measurement. The retrieved value in this example yields 295.3 K within .2 K of in situ surface skin hat measurements (Smith *et al*, 1995). The atmospheric reflection correction is comparable to the correction from the reduced surface emittance.

7.4 Estimating Fire Size and Temperature

The most practical and economically feasible manner of monitoring the extent of burning associated with tropical deforestation and grassland management is through remote sensing. To date, many remote sensing methods have utilized multispectral data from the Multispectral Scanner (MSS) on Landsat-1, -2, . . . -5, the Thematic Mapper (TM) on Landsat-4 and -5, and the Advanced Very High Resolution Radiometer (AVHRR) on the NOAA polar orbiters (Tucker *et al*, 1984; Matson and Holben, 1987; Nelson *et al*, 1987; Malingreau and Tucker, 1988). A number of these techniques calculate vegetative indices in order to estimate deforestation areas (Justice *et al*, 1985; Malingreau *et al*, 1985; Townshend *et al*, 1987). However, the extent of deforestation is usually

underestimated, mostly due to the inability to distinguish between primary and secondary growth (Malingreau and Tucker, 1988).

Another estimation of the rate of deforestation can be made by monitoring biomass burning. Matson and Dozier (1981) developed a technique utilizing the AVHRR 3.7 micron and 10.8 micron channels to detect subpixel resolution forest fires. The technique provides reasonable estimates of temperature and area of fires in those 1 km pixels that are not saturated (Matson and Holben, 1987). Unfortunately, many of the pixels are saturated and it is difficult to monitor plume activity associated with these subpixel fires, since the NOAA polar orbiting satellite has only one day time pass over a given area. The Geostationary Operational Environmental Satellite offer continuous viewing and less pixel saturation (because the pixel resolution is 4 km on GOES-8 or 16 km on GOES-7). Furthermore, the fire plumes can be tracked in time to determine their motion and extent. Thus the GOES satellite offers a unique ability to monitor diurnal variations in fire activity and transport of related aerosols.

The different brightness temperature responses in the two infrared window channels can be used to estimate the temperature of the target fire as well as the subpixel area it covers. Typically, the difference in brightness temperatures between the two infrared windows at 3.9 and 11.2 microns is due to reflected solar radiation, surface emissivity differences, and water vapour attenuation. This normally results in brightness temperature differences of 2-4 K. Larger differences occur when one part of a pixel is substantially warmer than the rest of the pixel. The hotter portion will contribute more radiance in shorter wavelengths than in the longer wavelengths. This can be seen in Figure 7.6 which depicts a portion of a line of VAS data over South America at 1831 UTC on 24 August 1988. Pixels a, b, and c represent areas where subpixel fires are burning. The largest temperature difference occurs at location b where the 11 micron brightness temperature value is 306.2 K and the 4 micron brightness temperature is 321.4 K. Warm areas surrounding these pixels are previously burned regions.

The fire extent and temperature within a field of view can be determined by considering the upwelling thermal radiance values obtained by both channels (Matson and Dozier, 1981; Dozier, 1981). For a given channel, λ , the radiative transfer equation indicates

$$R_{\lambda}(T) = \varepsilon_{\lambda} B_{\lambda}(T_s) \tau_{\lambda}(s) + \int_0^1 B_{\lambda}(T) d\tau_{\lambda}$$

When the GOES radiometer senses radiance from a pixel containing a target of blackbody temperature T_t occupying a portion p (between zero and one) of the pixel and a background of blackbody temperature T_b occupying the remainder of the pixel (1- p), the following equations represent the radiance sensed by the instrument at 4 and 11 micron.

$$R_4(T_4) = p R_4(T_t) + \varepsilon_4 (1-p) R_4(T_b) + (1-\varepsilon_4) \tau_4(s) R_4(\text{solar})$$

$$R_{11}(T_{11}) = p R_{11}(T_t) + \varepsilon_{11} (1-p) R_{11}(T_b)$$

The observed short wave window radiance also contains contributions due to solar reflection that must be distinguished from the ground emitted radiances; solar reflection is estimated from differences in background temperatures in the 4 and 11 micron channels. Once T_b is estimated from nearby pixels, these two nonlinear equations can be solved for T_t and p . In this study, the solution to the set of equations is found by applying a globally convergent bisection technique followed by Newton's method.

Atmospheric correction implicit in these equations are important. Burning or smoldering fires are usually covered by clouds and smoke containing organic particles of varying sizes and shapes, necessitating a correction to the transmittance. Most of the smoke is composed of water vapour, but there are other constituents as well (Andreae *et al*, 1988; Browell *et al.*, 1988). The 11 micron channel is more affected by atmospheric water vapour than the 4 micron channel. With

Nimbus-2 data, it was found that the water vapour correction for a moist atmosphere is approximately 4 K at 300 K for the 11 micron window and 2 K at 300 K for the 4 micron window (Smith *et al*, 1970). By calculating a linear regression relationship between the GOES visible brightness counts and GOES infrared window brightness temperature in a variety of haze conditions (approximately 50) and extrapolating to clear sky conditions, the Nimbus corrections were found to be appropriate for the GOES data studied (Prins and Menzel, 1994).

Emissivity investigations for vegetation similar to that found in the selva and cerrado suggest an emissivity for tropical rainforest of .96 in the 4 micron region and .97 in the 11 micron region, while the emissivity of dry grassland is .82 and .88 respectively (American Society of Photogrammetry, 1983).

The algorithm proceeds as follows. A fire is identified and a nearby fire free area is located. All observed brightness temperatures over the fire are adjusted for smoke attenuation; 2 K is added to the 4 micron brightness temperatures and 4 K is added to the 11 micron brightness temperatures. T_4 and T_{11} represent the smoke corrected brightness temperatures over the fire for the two spectral bands. The background temperature, T_{b11} , is determined from the 11 micron brightness temperature in a nearby fire-free pixel ($p=0$) that is adjusted for surface emissivity. Subsequently, the shortwave window reflected radiance for this same fire-free pixel, R_{4solar} , is solved. The input parameters T_{b11} , T_4 , T_{11} , and R_{4solar} are now all in place; thus the equations can be solved for p and T_t (Prins and Menzel, 1994).

The process of fire identification is strongly dependent on image interpretation. A fire was suspected if the haze corrected 3.9 micron observed brightness temperature showed a 4 K increase over the 3.9 micron background temperature and the haze corrected 11.2 micron observed temperature displayed a 1 K increase above the 11.2 micron background temperature. Hot spots were not considered fires unless they were accompanied by some indication of a fire in the visible channel, such as a smoke plume. The temporal resolution of the GOES data is extremely useful in two ways. First, a hot spot is often evident in the infrared channels at a certain time period, but the corresponding visible channel showed little or no indication of a fire, possibly due to obscuration by a plume produced by a fire located upwind. A visible image a half hour earlier usually clarified whether a fire is located there. Second, it is difficult to distinguish regular clouds from plumes in a single image. By looping a series of half hourly visible images it is quite easy to identify the point sources of fires, since they remain at a constant location over time.

In South America GOES-8 is being used to continue monitoring trends in biomass burning and to catalogue the extent and transport of associated aerosols. The Automated Biomass Burning Algorithm (ABBA) developed by Prins and Menzel (1994) was used to monitor the 1995 biomass burning season in South America with GOES-8. Multi-spectral diurnal imagery (3-hourly) were collected from June through September to provide a clear picture of biomass burning activities throughout the burning season including estimates of sub-pixel size and mean temperature and information on smoke/aerosol transport. Preliminary GOES-8 ABBA results obtained during the Smoke, Clouds, and Radiation (SCAR-B) experiment in Brazil (15 August - 15 September 1995) suggest that the peak burning time is in the middle of the afternoon (1800 UTC). Figure 7.7 shows that the number of fires detected near 1800 UTC is 2 times greater than that observed 3 hours earlier or later and 8 times greater than that observed at 1200 UTC. The majority of the fire activity is concentrated along the perimeter of the Amazon in the Brazilian states of Para, Mato Grosso, Amazonas, and Rondonia. There is also considerable activity in Bolivia, Paraguay, and Northern Argentina. Compared to GOES-VAS, the improved spatial resolution available with GOES-8 provides much greater detail concerning fire activity and other surface features. During SCAR-B smoke was evident over a large portion of the continent east of the Andes Mountains in the GOES visible images. A large smoke pall covering over 4 million km^2 was observed from 21 August through 11 September. Figure 7.8 indicates that at the height of this burning period the smoke pall extended over nearly 7 million km^2 . Transport over the Atlantic Ocean was observed on 13 days during the SCAR-B field program. On at least two days a thin plume of smoke was tracked to the Prime Meridian.

Table 7.1: Surface Skin Temperature regression relationships expressed as a Linear Combination of Infrared Window Brightness Temperatures, $T_s = A_0 + \sum A_i T_{bi} + \sum B_i (\Delta T_{bi})^2$. The root mean square (RMS) of the fit with respect to buoy reports is also indicated.

GOES Imager on GOES-8

A0	A(11.0)	A(12.0)	B(11.0-12.0) ²	RMS
-6.411	2.2160	-1.1900	0.2017	0.7 K

GOES Imager on GOES-9

A0	A(11.0)	A(12.0)	B(11.0-12.0) ²	RMS
-6.9510	2.8200	-1.7927	0.0756	0.7 K

AVHRR on NOAA-12

A0	A(11.0)	A(12.0)	RMS
10.11	3.5428	-2.5792	0.6 K

AVHRR on NOAA-14

A0	A(11.0)	A(12.0)	RMS
-5.31	3.1569	-2.1396	0.6 K

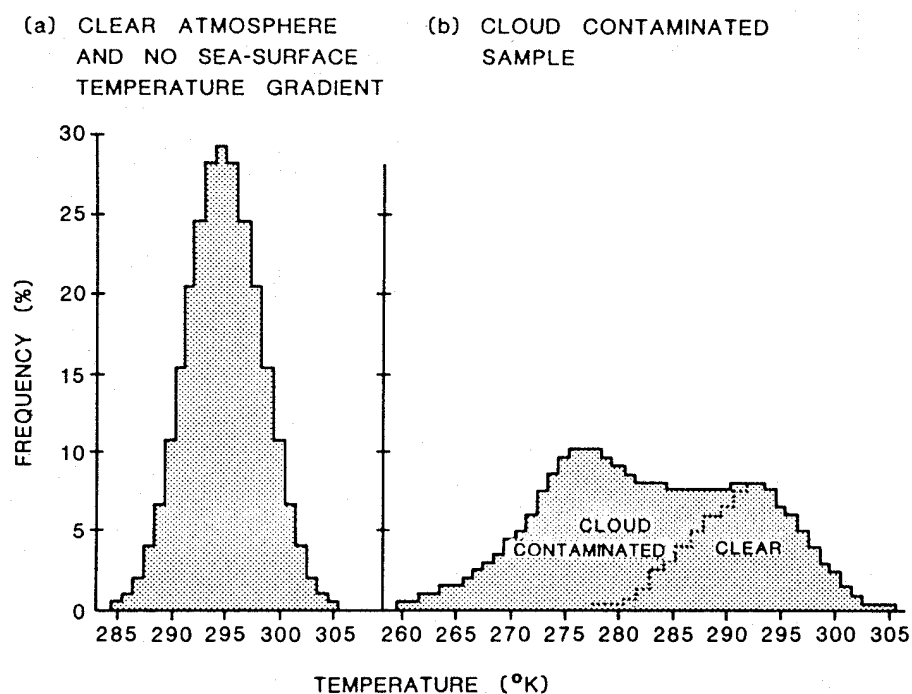


Figure 7.1: Histograms of infrared window brightness temperature in cloud free and cloud contaminated conditions.

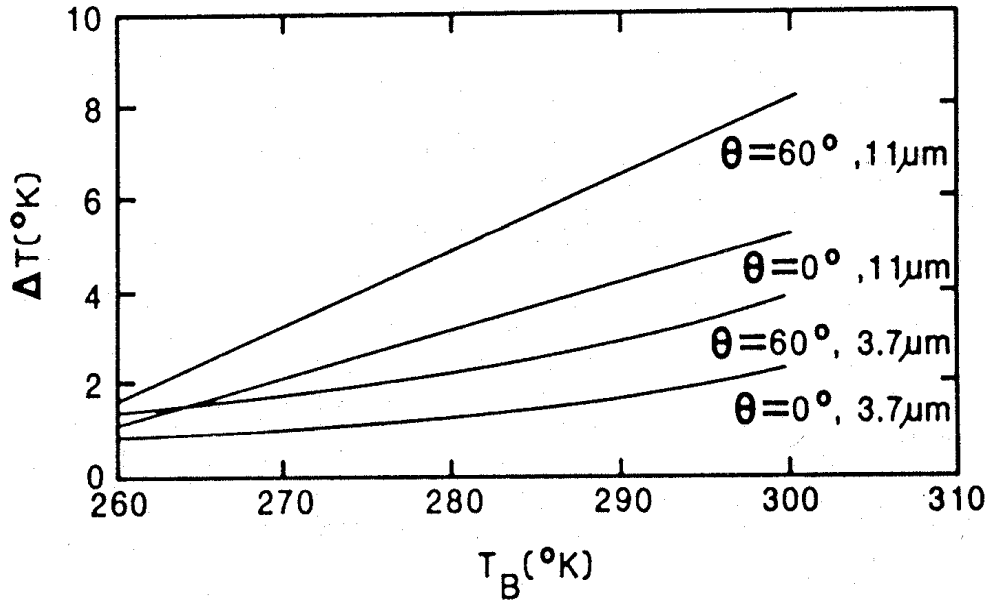


Figure 7.2a: Statistical relations of the water-vapour correction as a function of observed brightness temperature for two spectral channels and two viewing angles.

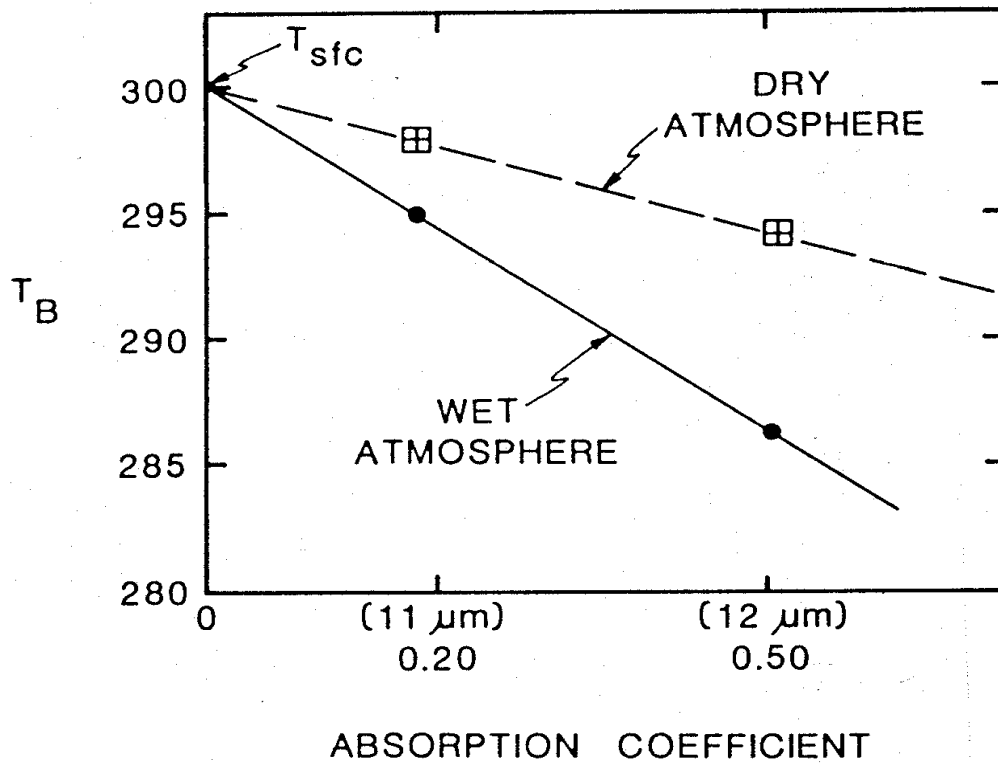


Figure 7.2b: Graphic representation of the linear relation between water vapour attenuation and brightness temperature for two different atmospheric conditions.

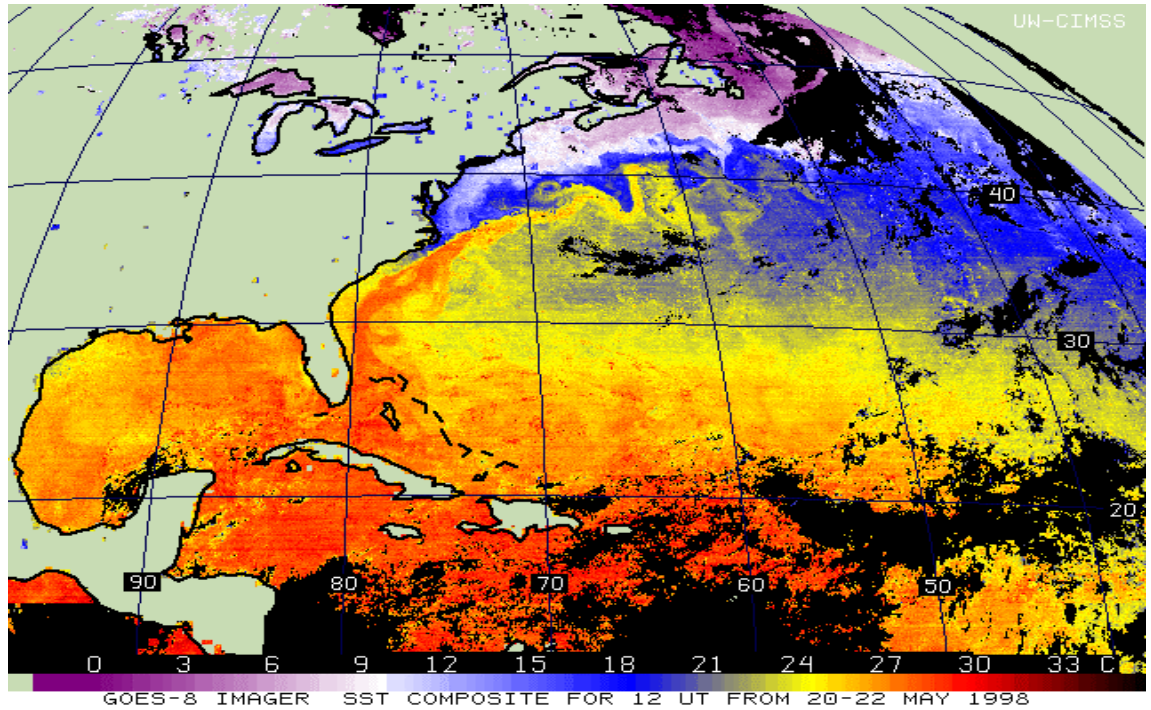


Figure 7.3a: Three-day composite of 1200 UTC GOES SST (early morning), May 20-22, 1998.

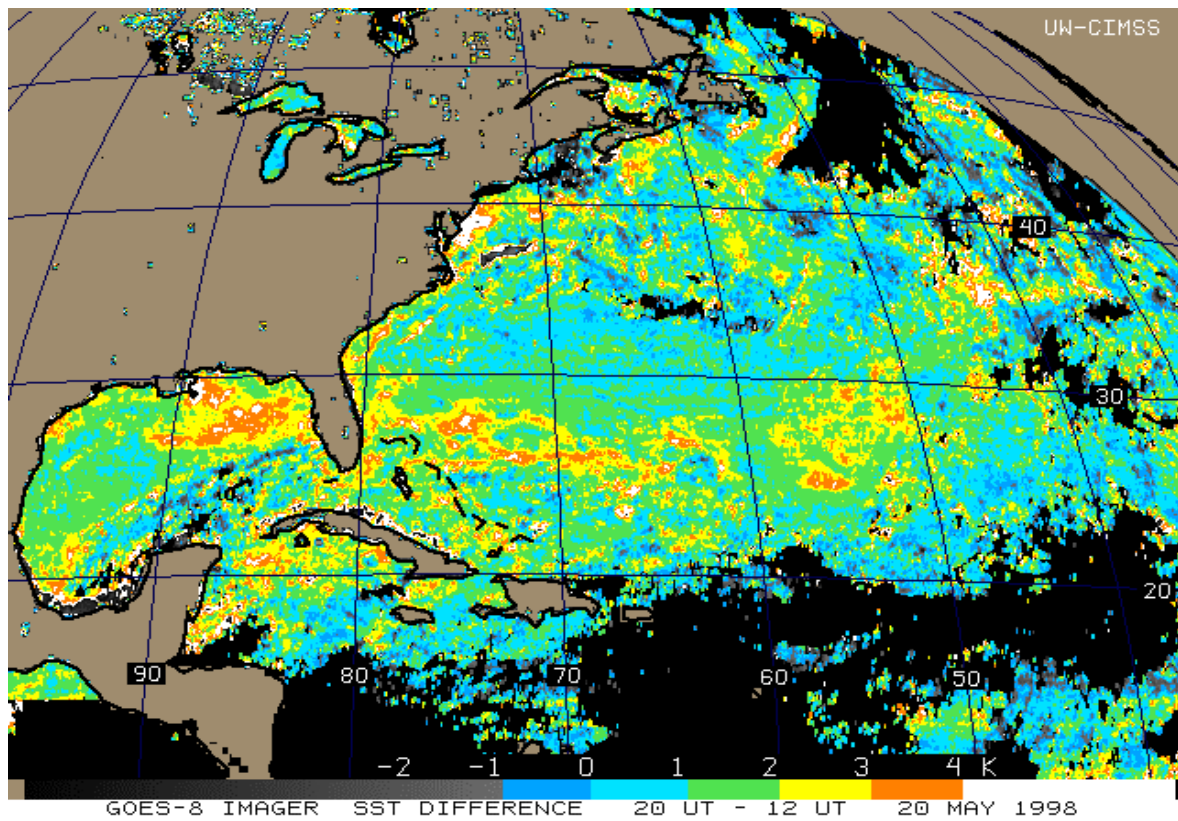


Figure 7.3b: Three-day composite of the difference in the GOES SST at 2000 UTC (afternoon) and 1200 UTC (early morning) for May 20-22, 1998. Differences greater than 3 K occur in clear skies in the tropics where the surface winds are less than 5 m/s (hence the ocean is relatively smooth).

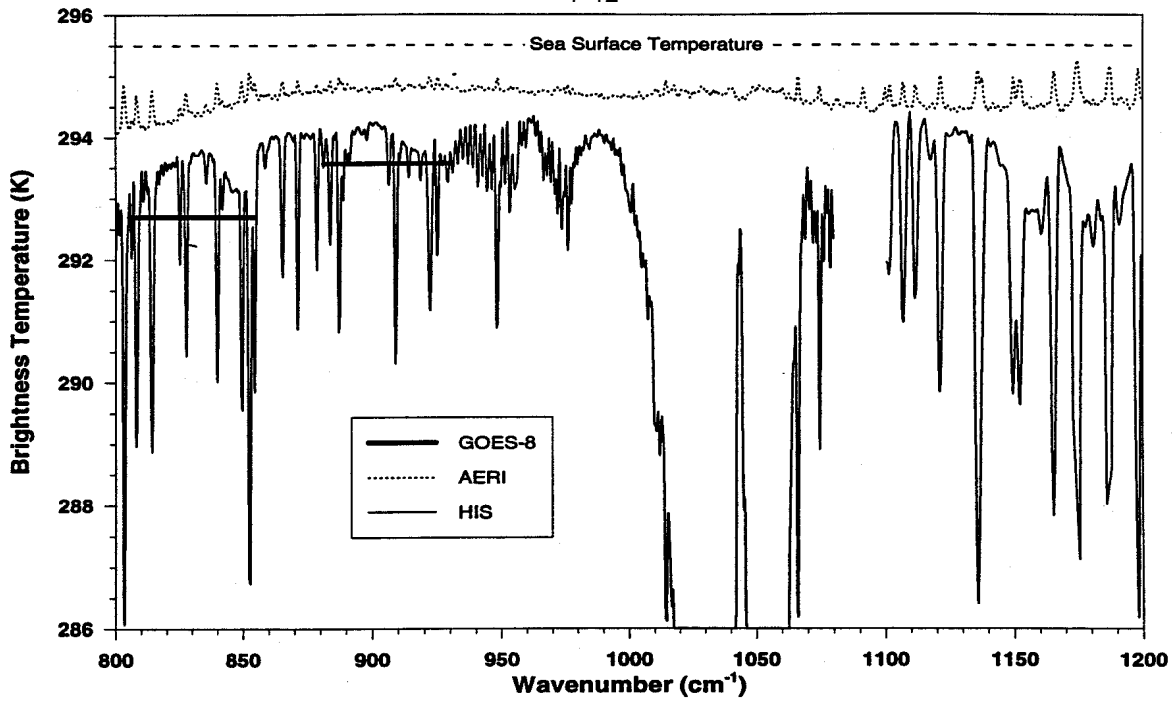


Figure 7.4: Comparison of ocean brightness temperatures measured by a ship borne interferometer (AERI), by an interferometer (HIS) on an aircraft at 20 km altitude, and the geostationary sounder (GOES-8). Corrections for atmospheric absorption of moisture, non-unit emissivity of the sea surface, and reflection of the atmospheric radiance from the sea surface have not been made.

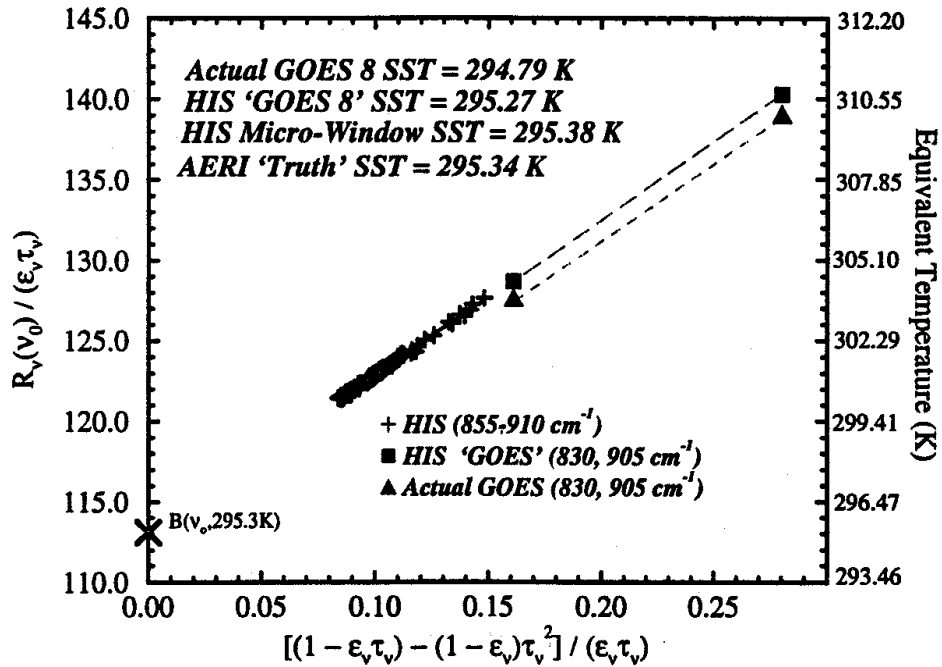


Figure 7.5: HIS and GOES radiance observations plotted in accordance with the radiative transfer equation including corrections for atmospheric moisture, non-unit emissivity of the sea surface, and reflection of the atmospheric radiance from the sea surface. Radiances are referenced to 880 cm⁻¹. The intercept of the linear relationship for each data set represents a retrieved surface skin blackbody radiance from which the SST can be retrieved.

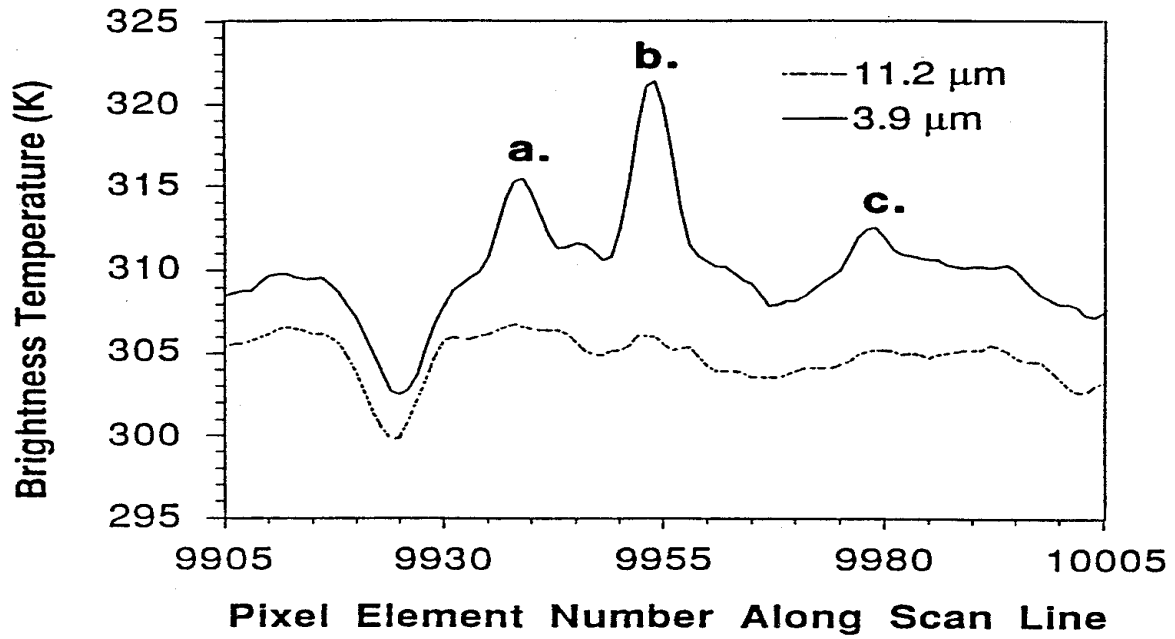


Figure 7.6: GOES VAS brightness temperatures at 3.9 and 11.2 microns plotted for one scan line over grassland burning in South America.

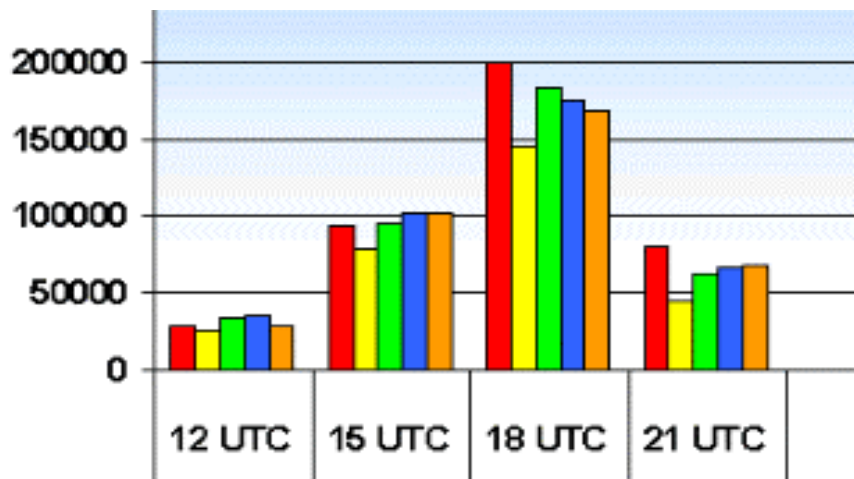


Figure 7.7: Diurnal variation in the detection of biomass burning in South America (number of fires) with GOES-8 for 1995 (red), 1996 (yellow), 1997 (green), 1998 (blue), and 1999 (brown). Prominent daily peak at 1800 UTC is evident.

Preliminary Estimates of Daily Smoke Coverage Observed in
GOES-8 Imagery During the 1995 SCAR-B Field Program

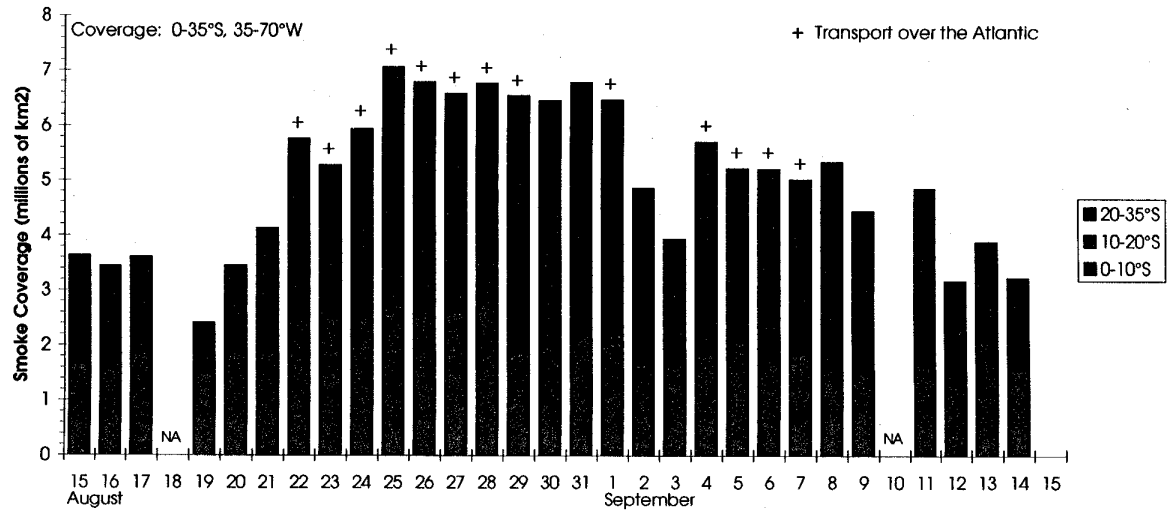


Figure 7.8: Estimates of daily smoke coverage over South America observed in GOES-8 visible imagery during August-September 1995.